Results in Physics 6 (2016) 170–177

Contents lists available at ScienceDirect

Results in Physics

journal homepage: www.journals.elsevier.com/results-in-physics

Skeleton-based tracing of curved fibers from 3D X-ray microtomographic imaging

Xiang Huang [a,*], Donghui Wen [a], Yanwei Zhao [a], Qinghui Wang [b], Wei Zhou [c], Daxiang Deng [c]

[a] School of Mechanical Engineering, Zhejiang University of Technology, Hangzhou 310014, China
[b] School of Mechanical and Automotive Engineering, South China University of Technology, Guangzhou 510640, China
[c] Department of Mechanical & Electrical Engineering, Xiamen University, Xiamen 361005, China

ARTICLE INFO

Article history:
Received 19 February 2016
Accepted 18 March 2016
Available online 25 March 2016

Keywords:
Fiber tracing
Skeleton
Morphology analysis

ABSTRACT

A skeleton-based fiber tracing algorithm is described and applied on a specific fibrous material, porous metal fiber sintered sheet (PMFSS), featuring high porosity and curved fibers. The skeleton segments are firstly categorized according to the connectivity of the skeleton paths. Spurious segments like fiber bonds are detected making extensive use of the distance transform (DT) values. Single fibers are then traced and reconstructed by consecutively choosing the connecting skeleton segment pairs that show the most similar orientations and radius. Moreover, to reduce the misconnection due to the tracing orders, a multilevel tracing strategy is proposed. The fibrous network is finally reconstructed by dilating single fibers according to the DT values. Based on the traced single fibers, various morphology information regarding fiber length, radius, orientation, and tortuosity are quantitatively analyzed and compared with our previous results (Wang et al., 2013). Moreover, the number of bonds per fibers are firstly accessed. The methodology described in this paper can be expanded to other fibrous materials with adapted parameters.

Introduction

Porous fibrous media have received increased attention in the past decade because of their easy manufacture (compared with foam materials) and growing use in most areas of science and engineering due to their excellent mechanical and transport properties. Recently, a promising fibrous material, PMFSS [1] was successfully manufactured and applied in fuel cell as crystal support layer in methanol stream reforming. Its unique fibrous architecture and high surface volume ratio were experimentally demonstrated to dramatically improve the production rate of hydrogen [2]. It's generally accepted that the macroscopic performance of the fibrous functional material is in deep correlation with the microstructure. To characterize the microstructure of PMFSS, in our previous work, various structural information of PMFSS concerning fiber segment orientation, length distribution, tortuosity, etc. were quantitatively investigated based on the extracted skeleton representation of the fiber structure extracted from the 3D X-ray images [3].

However, the optimization design of PMFSS needs further characterization of the arrangement of each individual fiber, rather than the fiber segments divided by fiber to fiber bonds. It is because the virtual fibrous material is generally created as the accumulation of individual fibers [4]. Unfortunately, owing to the nature of copper fibers and manufacturing process involving mold pressing and sintering, fibers in PMFSS are plastically deformed into various curved shapes with fiber bonds formed at contact regions, which increase the difficulty of identification of individual fibers.

Several approaches of tracing and identifying single fibers in fibrous material have been proposed taking advantages of various structural characteristics. Tessmann et al. [5] traced the fiber segments from tomographic 3D data of fibrous material composed of fibers with a unique diameter, the Hessian matrix of each voxel (pixel in 3D) was computed to estimate local orientations, fiber paths were finally reconstructed and tracked by connecting voxels with the minimum eigenvectors. Latil et al. [14] detected almost parallel fibers with convex cross sections. Adjoining fiber cross sections on the 2D slice image were separated using the watershed algorithm. More recently, Jerome [6] proposed a skeleton-based fiber segmentation algorithm to deal with low density materials. An extensive use of the DT method was applied to facilitate the identification of spurious segments due to the image noises and linking segments at fiber connecting joints. The remaining paths showed the most similar radius and orientation deviation was connected and merged under a parameterized criterion. Meanwhile,

* Corresponding author. Tel./fax: +86 20 88320717.
E-mail address: 522250912@qq.com (X. Huang).

http://dx.doi.org/10.1016/j.rinp.2016.03.008
2211-3797/

Gaiselmann et al. [7,8] extracted curved fibers of non-woven materials. The skeleton voxels with more than 3 neighbors were removed, and the remaining voxel paths were then vectorised into polygonal tracks. These tracks were later connected on either side which made balance between the deviation of angles and the distances. In addition, taking advantage of the same diameter of fibers, fiber bundles composed of parallel adjacent fibers were distinguished according to the DT values instead of misidentifying them as one single fiber.

It turns out that the most critical process in fiber tracing is the detection of the appropriate connecting fiber segment pairs, particularly in curved fibers. Thus, various tracing criterions were proposed [6–8] which aimed at achieving the correct segment links. In this work, we explore the efficient fiber tracing method adapted to our fibrous material, PMFSS. Instead of the complex parameterized tracing criterions used in existing methods [6–8], we reduce all affect factors (deviation of diameters, segment orientations, etc.) into one single parameter, the punishing angle, which is easier to understand and implement. Moreover, a multilevel tracing strategy is also proposed, which could effectively reduce the misconnection caused by the tracing orders. Finally, a further morphology exploration of PMFSS is performed according to the traced single fibers.

Materials and methods

Manufacture and micro-CT scans of PMFSS

The methodology of manufacture and microstructural characterization of PMFSS has been fully described in our previous studies [3]. Generally, after the cutting of continuous copper fibers and subsequent sintering and generation of PMFSS, its 3D images are obtained employing X-ray tomography. After a series of image processing involving selection of ROI, image enhancement of anisotropic diffusion [9] and binaryzation, the skeleton extraction is performed to obtain a topologically identical representation of the fiber structure. Fig. 1a shows the optical photographs of PMFSS samples with 90 porosity, and Fig. 1b shows the 3D geometrical reconstruction of ROI. Additionally, the porosity of PMFSS can be calculated with the mass–volume method as follows [1]:

$$E(\%) = \left(1 - \frac{M_p}{\rho_c V_p}\right) \times 100 \tag{1}$$

where V_p is the volume of PMFSS; M_p is the mass of PMFSS; ρ_c is the density of red copper.

Skeleton and segmentation

The skeletonization of fiber network in 3D binary image is computed using the thinning method [10] based on the DT method [11] and improved by introducing the scale axis transform method [12]. Once the skeleton was obtained, the voxels in skeleton were divided into three groups with respect to the 26-neighborhood of voxel (Fig. 2).

(1) End point, voxels with only one 26-neighborhood.
(2) Curve point, voxels with two 26-neighborhoods.
(3) Junction point, voxels with more than two 26-neigborhoods.

The skeleton network was then segmented into three groups of skeleton segments according to the three types of voxels:

(1) B–B path, both of the two end points are junction points.
(2) B–L path, one is an end point and the other is a junction point.
(3) L–L path, both of the two end points are end points.

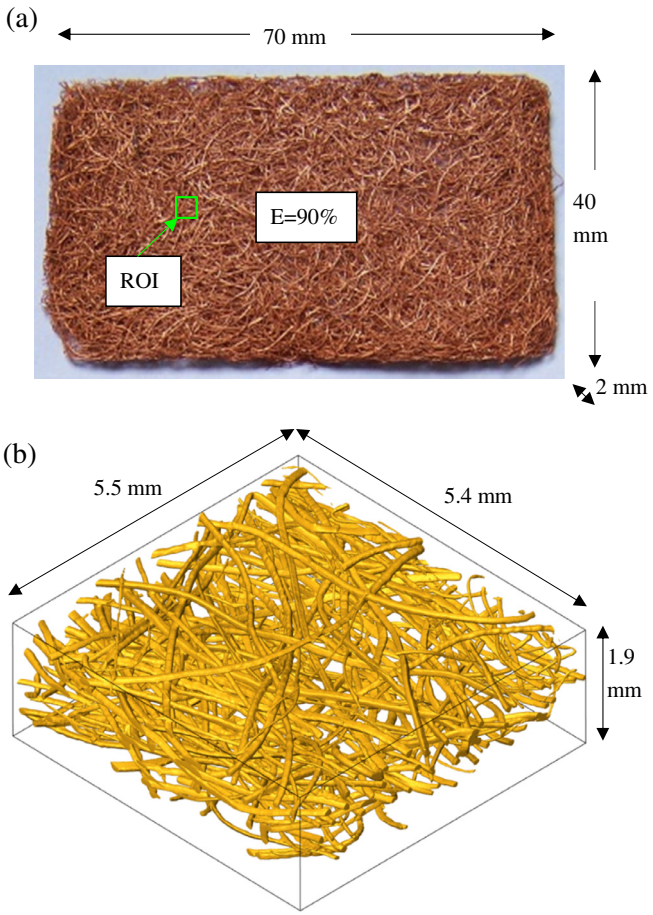

Fig. 1. (a) Optical photograph of PMFSS with 90% porosity sizing 40 × 70 × 2 mm and (b) 3D reconstructed geometrical visualization of ROI sizing 572 × 587 × 205 voxels, 1 pixel = 9.4 μm.

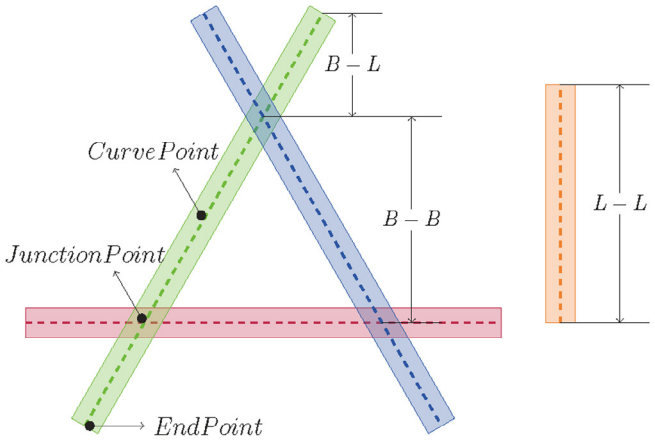

Fig. 2. Illustrations of categories of skeleton voxels and segments determined according to the categorized voxels.

Consequently, short B–L paths with length equal to the mean fiber radius were classified as spurs and removed. These B–L paths are mostly artificial segments due to the effect of digitization near the fiber surfaces. Fig. 3b shows the segmented skeletons of ROI sizing 200 × 200 × 50 with segments distinguished using different colors. The geometrical reconstruction of ROI is shown in Fig. 3a.

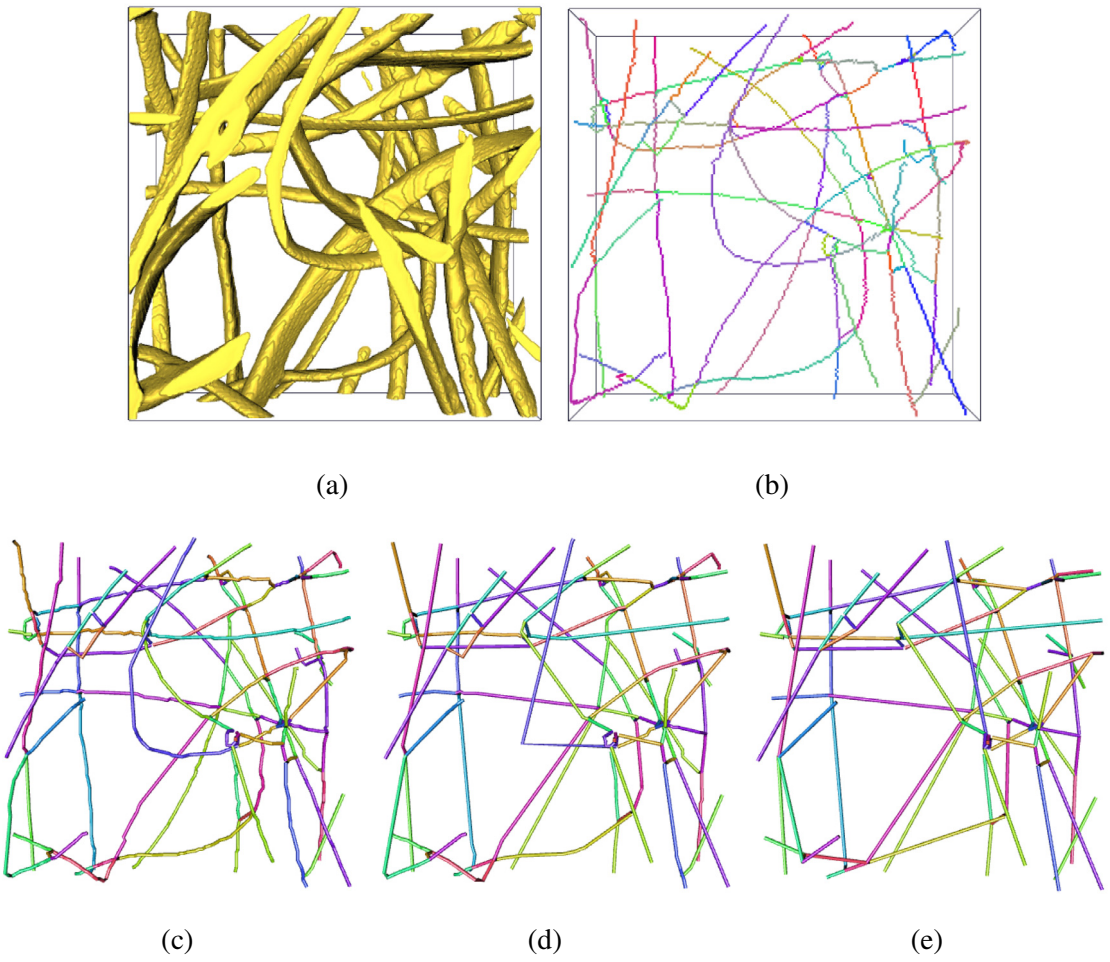

Fig. 3. Impacts of different tortuosity values on the vectorised skeleton segments (a) 3D reconstructed geometrical visualization of ROI sizing 200 × 200 × 50 voxels (b) the segmented skeletons representation, and the vectorised polygonal tracks obtained by the tortuosity values (c) 1.1 (d) 1.2 and (e) 2, respectively.

Vectorization

The connected skeleton segments were then transformed into vectorised polygonal tracks. The transformation is done as follows. For each fiber segment, starting from its one endpoint, and labeling it as the start point, the voxel-path distance between the current point and the start point is compared to the straight line distance between the two points. If the discrepancy between the two distances is too big, in other words, the tortuosity value is too big, the current point is recorded as the endpoint and, simultaneously, updated as the new start point of the next polygonal track. This procedure is repeated until the other end point of the fiber segment is reached. It's notable that the most crucial polygonal tracks located at both sides of the segment, which reflect the orientation trends at both sides. Hence, the polygonal tracks at both sides, as polygonal tracks P1-head and P1-tail of segment S1 shown in Fig. 4, are calculated separately for the accuracy of the following segment tracing. To find the appropriate tortuosity value for vectorization, a set of values were tested on ROI sizing 200 × 200 × 50 by voxel. Fig. 3c–e demonstrate the impacts of different tortuosity values (1.1, 1.2, 2) on the polygonal tracks respectively. As we can see, more delicate fiber course flection is preserved when the tortuosity value is lower, however, it will also make the polygonal tracks too sensitive to the fluctuation along the voxel courses, particularly near the fiber bonds. On the other hand, bigger tortuosity value, e.g., 2, may lose the curvature nature of some strongly curved fibers. Thus, in this work, a moderate value, 1.2, is selected.

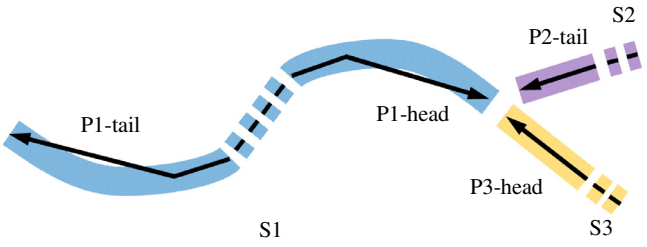

Fig. 4. Diagram of the vectorised segment skeletons. Three segments noted as S1, S2 and S3 are connected at the same node, and vectorised into polygonal tracks with the head and tail polygonal tracks (such as P1-tail and P1-head of S1, and for the rest segments as well) highlighted especially.

Detection of fiber bonding skeleton

The skeleton is topology identical to the original object, therefore, additional skeleton segments of B–B paths at the fiber bonds are preserved. During fiber tracing, we should avoid these artificial paths with lengths approximately equal to the sum of the radius of the two adjacent fibers. It was known in advance that the mean fiber diameter is 100 μm during manufacture, according to the 9.4 μm per voxel resolution, there are about 10 voxels within fiber's width. Actually, during detection, all suspicious segments of B–B path with lengths less than a bit above the mean fiber diameter (15 voxels) are checked according to their morphological features in the following three cases:

Segment with large deviation of DT values

Most of the fibers in PMFSS have nearly circular cross sections. Therefore, the DT values along each real fiber are approximately equal. However, the bonding skeleton is preferentially oriented perpendicularly to the two adjacent tubelike fibers. Thus, the DT values are bigger at its two extremes, which equal the radius of the two adjacent fibers, respectively, and the minimal DT value appears at the middle length where the surfaces of the tubelike fibers touch. The method for the detection of segments of this kind is as follows: $(1/4l < t < 3/4l)$, and $(vmax - vmin)/vmax > 0.5$, Where l is the length (number of voxels), t denotes the locate (voxel index) of the voxel with the minimal DT value, and *vmax* and *vmin* represent the maximal and minimal DT values of the suspicious segments, respectively. It's notable that the parameters in the criterion are chosen empirically which does well in our case.

Segment with small polar orientation angle

The 3D cross section images are parallel to the material plane (*xy*-plane) and stacked in the through thickness direction (*z* axis). Therefore, it's reasonable to assume that the suspicious segments with nearly vertical orientations are bonding segments between adjacent layers of fibers. The orientations are determined by the inertia matrix of the voxel representing skeleton as discussed in [3]. In this work, suspicious segments with a polar angle smaller than 40° (with 0° identical to the *z* axis) are categorized as bonding skeletons. The threshold angle is chosen empirically according to our material.

"H" type segment

Sometimes fibers with no-circular cross sections horizontally touches in *xy*-plane, and generate bonding segments which can't be detected directly using either DT values or orientations as explained in case (1) or (2). Generally, these B–B paths connected the adjacent two fibers like the middle line in character "H", where the end point of each B–B path divides each of the adjacent fibers into two nearly parallel polygonal tracks. Therefore, the straightness of the polygonal tracks of each local fiber, in other words, the angles between the polygonal tracks at both sides are evaluated, in particular, if both of the angles are bigger than a defined threshold value, e.g., 140°, we could consider the suspicious B–B path as a bonding segment. Fig. 5(a) highlights the detected artificial paths in Fig. 3(b) according to the above three cases.

Fiber tracing method and the multilevel tracing strategy

The polygonal track representing fiber segments are finally traced by connecting the adjacent polygonal tracks in the smoothest way. Firstly, for each fiber segment, its connecting and probably tracing tracks at both ends (head and tail) are detected, and two sets of possibly connecting polygonal tracks at both ends are generated, respectively. More precisely, two polygonal tracks (head or tail) of two different fiber segments are detected as adjacent neighbors if their end voxels are in 3 * 3 * 3 voxel region. Obviously, there can be more than one possibly connecting polygonal track as shown in Fig. 4. Thus, a decision rule has to be established which determines the most appropriate connecting segment. Various rules have been proposed taking account of three morphological impact factors: fiber diameters [6], angular deviation [6,7], and Euclidean distance of two polygonal tracks [7]. In a word, the possibility of two fiber segments getting connected during tracing increases if the deviation of the two fiber diameters is smaller, the angular deviation is closer to 0° or 180°, and the distance between the end voxels of two polygonal tracks is smaller. Despite the complex criterions used in [6,7], where different weighting parameters were imposed on these impact factors and normalized for comparison, indeed, all these efforts are contributed to one single goal, that is, the less possibly connected fiber segments are additionally penalized. Therefore, in this paper, these morphological impact factors are reduced to one single factor: the punishing angle. More precisely, the connection is punished by subtracting a punishing angle, e.g., 60°, from the actual angle deviation if the difference of segment diameters is big enough, or the candidate tracing segment is categorized as a fiber bonding skeleton according to the three cases. Specifically, assuming the radius (mean distance value) for two connected fiber segments are r1 and r2, respectively, then, their connecting angle is punished if $|r1 - r2|/\max(r1, r2) > 0.5$, where symbol | | means the absolute value and max represents the maximal value. As mentioned above, all the parameters are chosen empirically.

A multi-level tracing algorithm is proposed in this paper. As showed in Fig. 4, supposing that segment s2 is the current tracing segment, the next connection would be segment s1 according to the angle deviation rule. However, it's obvious that segment pair s1 and s3 should be more proper configuration than segment pair s1 and s2. Thus, to prevent the misconnection due to the tracing order, a multi-level tracing algorithm is proposed with a minimal

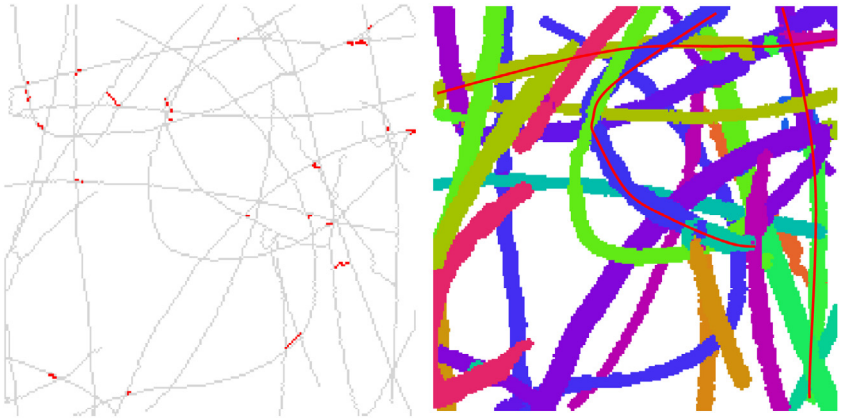

(a) (b)

Fig. 5. (a) Detected bonding skeletons highlighted in red according to the three cases. (b) Reconstructed with the traced individual skeletons by dilating the skeleton according to the DT values, and distinguished with different colors. The misconnected or broken skeleton is highlighted in red. (For interpretation of the references to color in this figure legend, the reader is referred to the web version of this article.)

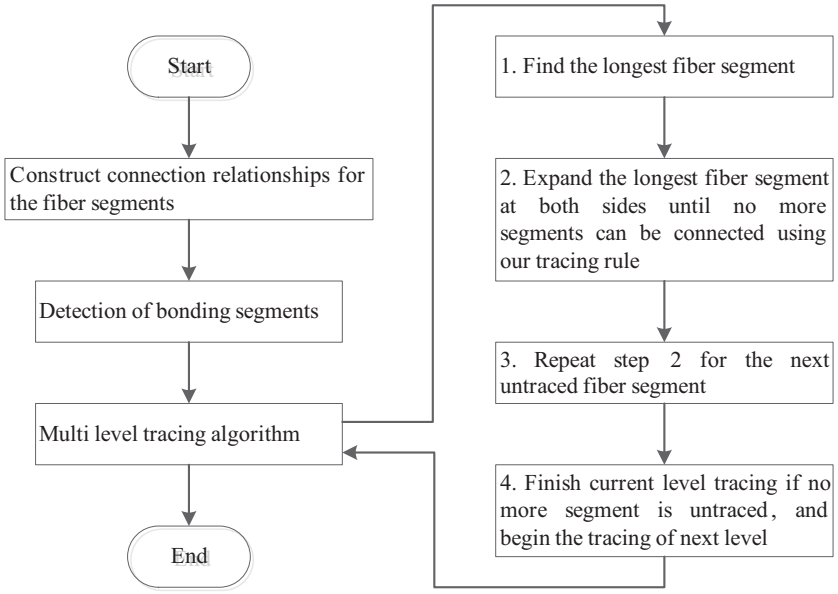

Fig. 6. Workflow of the multilevel fiber tracing algorithm.

angle deviation threshold set at each tracing level. More precisely, the angle deviation for the first tracing level is set close to 180°, e.g., 170°, and then reduces gradually at the following tracing levels (e.g., 140°, 100°, and 50°, respectively). Using this strategy, the polygonal track pairs with bigger angle deviation is traced preferentially. It's notable that better fiber configuration may achieve using more elaborate level settings, but at the expense of longer computation time, anyhow, satisfied visual result is obtained for our material using the four levels.

Finally, the fiber tracing algorithm begins from the longest untraced fiber segment. It is elongated at both sides according to the tracing rules until there are no more adjacent polygonal tracks or no tracks can satisfy the minimal angle deviation criterion at the current tracing level. Then, a single fiber is accomplished with all the segments of this single fiber labeled as traced and removed from the untraced list. This process is repeated until no more untraced segment is left, and the fiber tracing of the current level is finished. Then, the polygonal tracks of the fiber configuration at the current tracing level is updated and the tracing for the next level is processed as well. The flow chart of the overall fiber tracing algorithm is illustrated in Fig. 6.

Results and discussion

Two 3D volume datasets of PMFSS with 90% porosity were explored. The smaller one (sizing 200 × 200 × 50 voxels (Figs. 3 and 5)) demonstrates how the algorithm works and the bigger one (sizing 572 × 587 × 205 voxels (Figs. 1b and 7) is used for morphological analysis. To reconstruct the individual fibers and check the tracing accuracy, the traced skeleton is dilated by balls of radius equaling the distance values of each voxel along the fiber course. Fig. 5b shows the reconstructed individual fibers distinguished in different colors. As can be seen, most of the fibers are identified correctly. Some of the wrong (broken or misconnected) fibers as highlighted in red are caused by the skeleton architecture where fibers parallelly touch and merge into one skeleton instead of separate skeletons representing each fiber. However, such a skeleton merging situation seldom occurs in fibrous media of high porosity. In [8], the touched fibers with unique radius in a dense fiber network were distinguished by removing voxels with DT values below a certain threshold value. Finally, about 89% of fiber segments were traced correctly using optimized parameters. More precise segmentation was reported in [6] where fibers are shorter and deviation of fiber radius is bigger. It is notable that despite many precautions and a multilevel tracing strategy being applied, we can't assure the perfect parameter setting for all the fibers, especially fibers with long lengths, irregular cross sections, and big tortuosity. Fig. 7b shows the traced results of the bigger dataset, compared with the one (Fig. 7a) before tracing, it could be observed that the number of fiber segments reduces dramatically and most of the fibers are connected correctly along the fiber courses. Fig. 8 shows some selected single fibers from Fig. 7b, it demonstrates that there exists long fibers with various tortuosity and radius. In this work, to adequately capture the structural properties of the traced fibers, we only count single fibers with lengths larger than 50 voxels (about 5 times the length of mean fiber diameter). At last, all the distributions were measured based on the 213 identified single fibers from the bigger 3D volume dataset shown in Fig. 7b.

Distributions of single fiber lengths and radius

The fiber length distribution is shown in Fig. 9a. After the fiber tracing operation, long fibers appear and focus in range from 200 to 1500 voxel size (about 2–14 mm according to the 9.4 μm voxel resolution). The mean value of length is about 4.44 mm, and is approximately one order of magnitude as the value 0.43 mm reported in [13] for the same material before fiber tracing operation. Fig. 9b shows the distribution of fiber radius, the mean radius is 33 μm. Note that the value of radius is very sensitive to the shape of cross sections and the selection of fibers in respect to the fluctuation of cutting depth during turning process.

Fig. 9c shows the tortuosity measured on the fiber skeletons, it's observed that some very high tortuosity values appear. Actually, an extremely large value (155) was obtained and excluded from the statistics. Consequently, the mean value of tortuosity is about 1.78, and is bigger than the peak value 1.5 measured in [3] for PMFSS with 80% porosity. This result is reasonable as the tortuosity increases with the fiber getting longer while more twists and turns occur on its path.

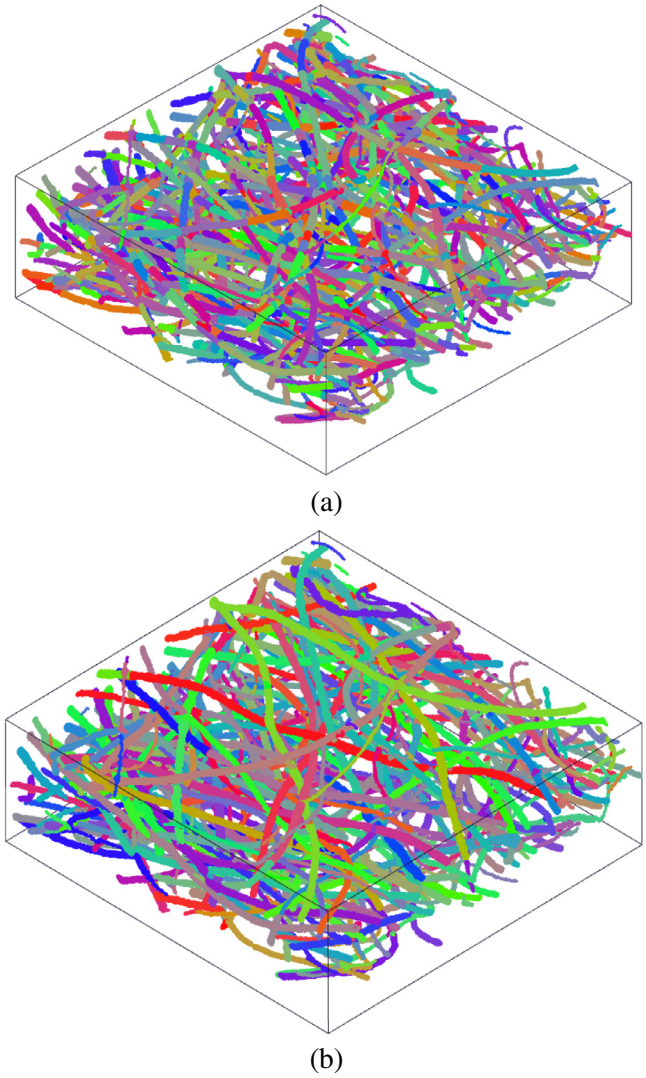

Fig. 7. (a) Reconstructed fiber network composed of fiber segments before fiber tracing, and (b) the reconstructed traced single fibers.

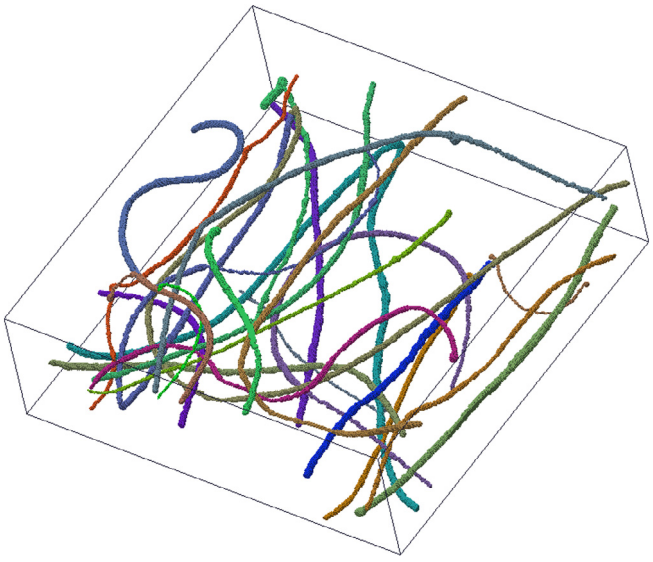

Fig. 8. A small portion of the selected single fibers from Fig. 7(b), it shows that PMFSS is composed of fibers with long length, various radius and tortuosity.

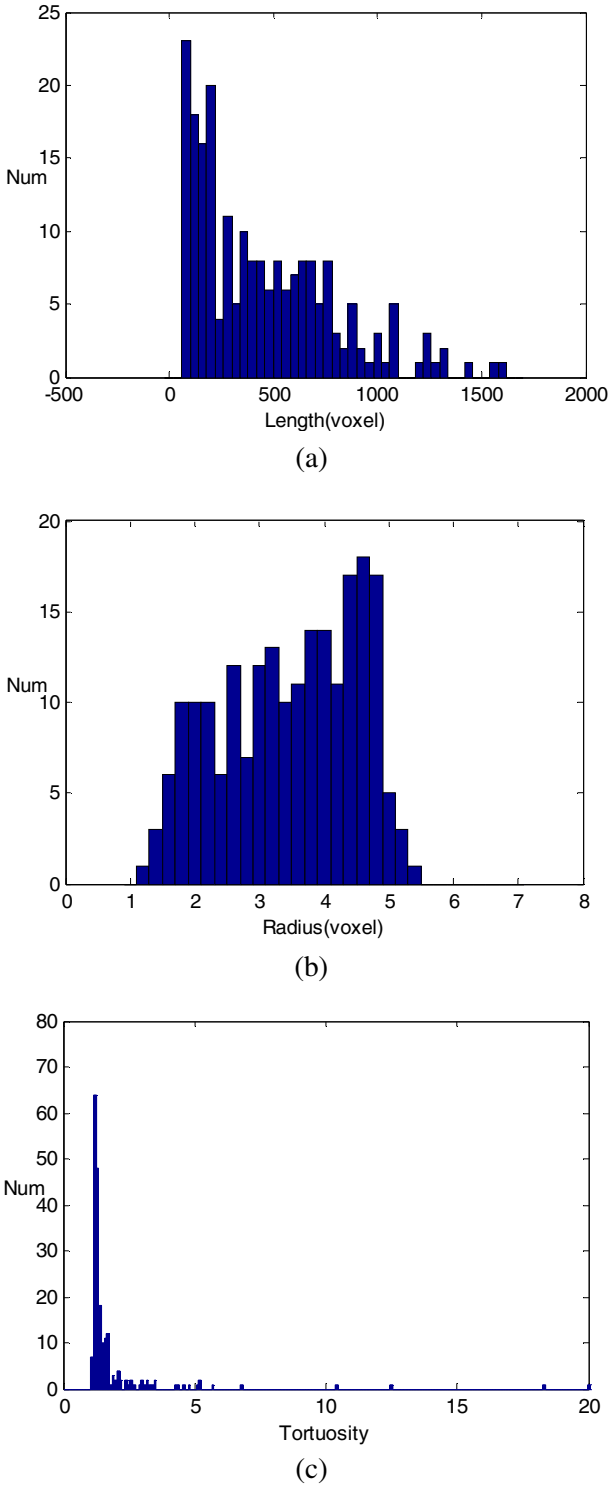

Fig. 9. Histogram of morphology characteristics of traced single fibers involving (a) length (b) radius and (c) tortuosity.

Distribution of fiber orientations and bonds per fiber

The orientation of fiber segments were deduced from the moment of inertia tensors in most works, with the smallest moment of inertia indicating the orientation [3]. However, this approach is only applicable when the tortuosity is small. Extremely, the deduced direction for geometry of circular shape that lies in *xy*-plane would be 45 degrees in polar angle according to the

direction of the smallest moment of inertia tensors, which is obviously wrong. Therefore, in this work, the direction is simplified as the orientation of the straight vector connecting the two extremes of single fiber. Fiber orientations are denoted as parameter φ in azimuth angle (0–360°) in *xy*-plane and θ in the polar angle (0–90°, with $\theta = 0°$ corresponding to the *z*-axis). As shown in Fig. 10a, it clearly reflects that PMFSS has a layered structure, as most fibers are oriented in the material plane (polar angle $\theta = 90°$). A slightly anisotropic orientation trend in azimuth angle is observed as well. To better study the orientation in *xy*-plane, an even bigger domain of 3D image and more powerful computing hardware are needed. At this moment, it's no doubt that the material quality, and especially the manufacture processes involving the loading and mold pressing will affect the fiber orientations.

The number of bonds of fibers was beyond measurement previously, after fiber tracing, this important structural characteristic is accessible. Fig. 10b demonstrates the distribution of bonds per fiber. The average number of bonds per fiber is 6.9, bigger than the value 3.7 reported in [6] where fibrous media is of close porosity but with smaller fiber aspect ratio (length to width). Fig. 10c emphasizes the number of bonds with respect to the fiber length. It clearly shows that the number of bonds is quite proportionate to the increase of fiber length. The distribution of fiber bonds is considered of critical importance that affects the mechanical strength, thermal and other transport properties.

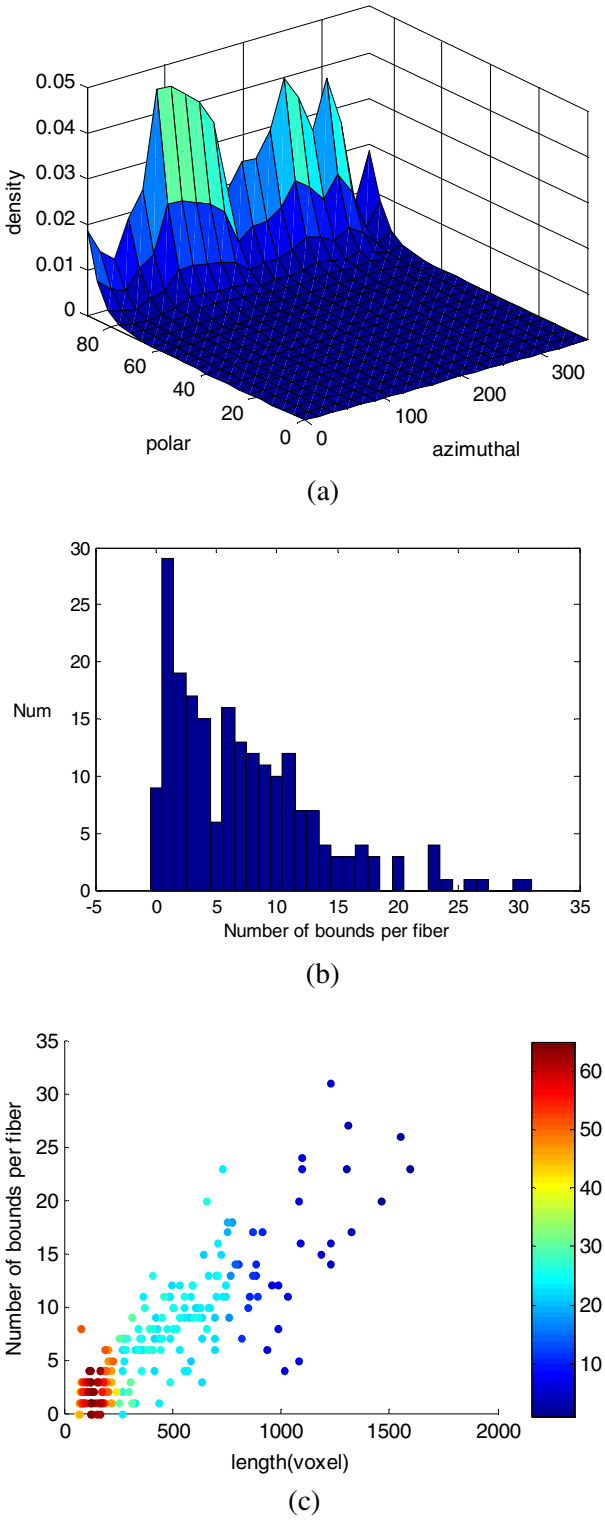

Fig. 10. Morphological statistical characteristics of traced single fibers involving (a) fiber orientations in 3D (b) number of bonds per fiber and (c) the relationship between the length and the number of bonds.

Conclusions

To extract single fibers from a specific fibrous porous material, PMFSS, a skeleton based multilevel tracing strategy is proposed. We firstly build the connection relationship of the skeleton representing fiber segments, then, segments representing bonds between touched fibers are identified and punished (reduce the probability of being connected) during fiber tracing. To facilitate the identification of fiber bonds and fiber segments with big radius difference, the DT value is extensively used. A multilevel tracing strategy is proposed that the more proper fiber segment pairs are considered preferentially despite the tracing orders. The quantitative morphological statistics reflect that PMFSS is constructed of layered fibers with long length and big tortuosity. Moreover, the bonds per fiber are discussed, which plays an important role in the mechanical and transport properties. The tracing method described in this paper can be expanded to other fibrous media with adapted parameters.

Acknowledgements

This work is financially supported by Nature Science Foundation of China (Grant Nos. 51505426 and 51275177), and the Open Fund of Key Laboratory of E&M (Zhejiang University of Technology), Ministry of Education & Zhejiang Province (No. 2014EP0012).

References

[1] Tang Y, Zhou W, Xiang JH, Liu WY, Pan MQ. An innovative fabrication process of porous metal fiber sintered felts with three-dimensional reticulated structure. Mater Manuf Process 2010;25:565–71.
[2] Zhou W, Wang QH, Li JR, Tang Y, Huang ZM, Zhang JP, et al. Hydrogen production from methanol steam reforming using porous copper fiber sintered felt with gradient porosity. Int J Hydrogen Energy 2015;40:244–55.
[3] Wang QH, Huang X, Zhou W, Li JR. Three-dimensional reconstruction and morphologic characteristics of porous metal fiber sintered sheet. Mater Charact 2013;86:49–58.
[4] Altendorf H, Jeulin D. Random-walk-based stochastic modeling of three-dimensional fiber systems. Phys Rev E 2011;041804.
[5] Teßmann M, Mohr S, Gayetskyy S, Hassler U, Hanke R, Greiner G. Automatic determination of fiber length distribution in composite material using 3D CT data. EURASIP J Adv Signal Process 2010;545030.
[6] Lux L. Automatic segmentation and structural characterization of low density fiberboards. Image Anal Stereol 2013;32:13–25.
[7] Gaiselmann G, Thiedmann R, Manke I, Lehnert W, Schmidt V. Stochastic 3D modeling of fiber-based materials. Comput Mater Sci 2012;59:75–86.
[8] Gaiselmann G, Manke I, Lehnert W, Schmidt V. Extraction of curved fibers from 3D data. Image Anal Stereol 2013;32:57–63.
[9] Perona P, Malik J. Scale-space and edge detection using anisotropic diffusion. IEEE Trans Pattern Anal Mach Intell 1990;12:629–39.

[10] Lee TC, Kashyp RL. Building skeleton models via 3-D medial surface/axis thinning algorithm. Graph Model Image Process 1994;56:462–78.
[11] Pudney C. Distance-ordered homotopic thinning: a skeletonization algorithm for 3D digital images. Comput Vision Image Understanding 1998;72:404–13.
[12] Miklos B, Giesen J, Pauly M. Discrete scale axis representations for 3D geometry. ACM Trans Graph 2010;29:101:1–101:10.
[13] Huang X, Wang QH, Zhou W, Li JR. A simple fracture energy prediction method for fiber network based on its morphological features extracted by X-ray tomography. Mater Sci Eng A 2013;585:297–303.
[14] Latil P, Orgeas L, Geindreau C, et al. Towards the 3D in situ characterisation of deformation micro-mechanisms within a compressed bundle of fibres. Compos Sci Technol 2011;71:480–8.